



# The Second Catalog of Interplanetary Network Localizations of Konus Short-duration Gamma-Ray Bursts

D. S. Svinkin<sup>1</sup> , K. Hurley<sup>2</sup> , A. V. Ridnaia<sup>1</sup> , A. L. Lysenko<sup>1</sup> , D. D. Frederiks<sup>1</sup> , S. V. Golenetskii<sup>1</sup> , A. E. Tsvetkova<sup>1</sup> , M. V. Ulanov<sup>1</sup> , A. Kokomov<sup>1</sup> , T. L. Cline<sup>3</sup> , I. Mitrofanov<sup>4</sup> , D. Golovin<sup>4</sup> , A. Kozyrev<sup>4</sup> , M. Litvak<sup>4</sup> , A. Sanin<sup>4</sup> , A. Goldstein<sup>5</sup> , M. S. Briggs<sup>6</sup> , C. Wilson-Hodge<sup>7</sup> , E. Burns<sup>8</sup> , A. von Kienlin<sup>9</sup> , X.-L. Zhang<sup>9</sup> , A. Rau<sup>9</sup> , V. Savchenko<sup>10</sup> , E. Bozzo<sup>10</sup> , C. Ferrigno<sup>10</sup> , S. Barthelmy<sup>11</sup> , J. Cummings<sup>12</sup> , H. Krimm<sup>13</sup> , D. M. Palmer<sup>14</sup> , A. Tohuvavohu<sup>15</sup> , K. Yamaoka<sup>16</sup> , M. Ohno<sup>17,18,19</sup> , Y. Fukazawa<sup>20</sup> , Y. Hanabata<sup>20</sup> , T. Takahashi<sup>21,22</sup> , M. Tashiro<sup>23</sup> , Y. Terada<sup>23</sup> , T. Murakami<sup>24</sup> , K. Makishima<sup>25</sup> , W. Boynton<sup>26</sup> , C. W. Fellows<sup>26</sup> , K. P. Harshman<sup>26</sup> , H. Enos<sup>26</sup> , R. Starr<sup>27</sup> , J. Goldsten<sup>28</sup> , R. Gold<sup>28</sup> , A. Ursi<sup>29</sup> , M. Tavani<sup>29</sup> , A. Bulgarelli<sup>30</sup> , C. Casentini<sup>30</sup> , E. Del Monte<sup>29</sup> , Y. Evangelista<sup>29</sup> , M. Galli<sup>30,31</sup> , F. Longo<sup>32</sup> , M. Marisaldi<sup>30,33</sup> , N. Parmiggiani<sup>30</sup> , C. Pittori<sup>34,35</sup> , M. Romani<sup>36</sup> , F. Verrecchia<sup>34,35</sup> , D. M. Smith<sup>37</sup> , W. Hajdas<sup>38</sup> , S. Xiao<sup>39</sup> , C. Cai<sup>39</sup> , Q. B. Yi<sup>39</sup> , Y. Q. Zhang<sup>39</sup> , S. L. Xiong<sup>39</sup> , X. B. Li<sup>39</sup> , Y. Huang<sup>39</sup> , C. K. Li<sup>39</sup> , S. N. Zhang<sup>39</sup> , L. M. Song<sup>39</sup> , C. Z. Liu<sup>39</sup> , X. Q. Li<sup>39</sup> , W. X. Peng<sup>39</sup> , and I. Martinez-Castellanos<sup>40</sup>

<sup>1</sup> Ioffe Institute, Politekhnikeskaya 26, St. Petersburg, 194021, Russia  
<sup>2</sup> Space Sciences Laboratory, University of California, 7 Gauss Way, Berkeley, CA 94720-7450, USA  
<sup>3</sup> 13708 Sherwood Forest Drive, Silver Spring, MD 20904, USA

<sup>4</sup> Space Research Institute, 84/32 Profsoyuznaya, Moscow, 117997, Russia

<sup>5</sup> Science and Technology Institute, Universities Space Research Association, Huntsville, AL 35805, USA

<sup>6</sup> Space Science Department, University of Alabama in Huntsville, 320 Sparkman Drive, Huntsville, AL 35899, USA

<sup>7</sup> NASA Marshall Space Flight Center, Huntsville, AL 35812, USA

<sup>8</sup> Department of Physics & Astronomy, Louisiana State University, Baton Rouge, LA 70803, USA

<sup>9</sup> Max-Planck-Institut für extraterrestrische Physik, Giessenbachstrasse 1, D-85748 Garching, Germany

<sup>10</sup> Department of Astronomy, University of Geneva, Ch. d'Ecogia 16, 1290, Versoix, Switzerland

<sup>11</sup> NASA Goddard Space Flight Center, 8800 Greenbelt Road, Greenbelt, MD 20771, USA

<sup>12</sup> Center for Astrophysical Sciences, Johns Hopkins University, Baltimore, MD 21218, USA

<sup>13</sup> National Science Foundation, Alexandria, VA 22314, USA

<sup>14</sup> Los Alamos National Laboratory, B244, Los Alamos, NM 87545, USA

<sup>15</sup> Department of Astronomy and Astrophysics, University of Toronto, Toronto, ON, Canada

<sup>16</sup> Institute for Space-Earth Environmental Research (ISEE), Nagoya University, Furo-cho, Chikusa-ku, Nagoya 464-8601, Japan

<sup>17</sup> Institute of Physics, Eötvös University, Pázmány Péter sétány 1/A, Budapest, 1117, Hungary

<sup>18</sup> School of Science, Hiroshima University, 1-3-1 Kagamiyama, Higashi-Hiroshima, Hiroshima 739-8526, Japan

<sup>19</sup> Konkoly Observatory of the Hungarian Academy of Sciences, Konkoly-Thege ut 15-17, Budapest, 1121, Hungary

<sup>20</sup> Department of Physics, Hiroshima University, 1-3-1 Kagamiyama, Higashi-Hiroshima, Hiroshima 739-8526, Japan

<sup>21</sup> Department of Physics, The University of Tokyo, 7-3-1 Hongo, Bunkyo, Tokyo 113-0033, Japan

<sup>22</sup> Kavli Institute for the Physics and Mathematics of the Universe (WPI), The University of Tokyo Institutes for Advanced Study, The University of Tokyo, Kashiwa, Chiba 277-8583, Japan

<sup>23</sup> Department of Physics, Saitama University, 255 Shimo-Okubo, Sakura-ku, Saitama-shi, Saitama 338-8570, Japan

<sup>24</sup> Department of Physics, Kanazawa University, Kadoma-cho, Kanazawa, Ishikawa 920-1192, Japan

<sup>25</sup> Department of Physics, University of Tokyo, 7-3-1 Hongo, Bunkyo-ku, Tokyo 113-0033, Japan

<sup>26</sup> Lunar and Planetary Laboratory, University of Arizona, Tucson, AZ, USA

<sup>27</sup> Catholic University of America, Washington, DC 20064, USA

<sup>28</sup> Applied Physics Laboratory, Johns Hopkins University, Laurel, MD 20723, USA

<sup>29</sup> INAF/IAPS, via del Fosso del Cavaliere 100, I-00133 Roma (RM), Italy

<sup>30</sup> INAF/OAS, via Gobetti 101, I-40129 Bologna (BO), Italy

<sup>31</sup> ENEA Bologna, via don Fiammelli 2, I-40128 Bologna (BO), Italy

<sup>32</sup> Dipartimento di Fisica, Università di Trieste and INFN, via Valerio 2, I-34127 Trieste (TR), Italy

<sup>33</sup> Birkeland Centre for Space Science, Department of Physics and Technology, University of Bergen, Norway

<sup>34</sup> SSDC/ASI, via del Politecnico snc, I-00133 Roma (RM), Italy

<sup>35</sup> INAF/OAR, via Frascati 33, I-00078 Monte Porzio Catone (RM), Italy

<sup>36</sup> INAF—Osservatorio Astronomico di Brera, Via Brera, 28—I-20121 Milano (MI), Italy

<sup>37</sup> Physics Department and Santa Cruz Institute for Particle Physics, University of California, Santa Cruz, CA 95064, USA

<sup>38</sup> Paul Scherrer Institute, 5232 Villigen PSI, Switzerland

<sup>39</sup> Key Laboratory of Particle Astrophysics, Institute of High Energy Physics, Chinese Academy of Sciences, 19B Yuquan Road, Beijing 100049, People's Republic of China

<sup>40</sup> Department of Physics, University of Maryland, College Park, MD 20742, USA

Received 2021 October 28; revised 2021 December 1; accepted 2021 December 4; published 2022 March 16

## Abstract

We present the catalog of InterPlanetary Network (IPN) localizations for 199 short-duration gamma-ray bursts (sGRBs) detected by the Konus-Wind (KW) experiment between 2011 January 1 and 2021 August 31, which extends the initial sample of IPN-localized KW sGRBs to 495 events. We present the most comprehensive IPN

localization data on these events, including probability sky maps in Hierarchical Equal Area isoLatitude Pixelization format.

*Unified Astronomy Thesaurus concepts:* [Gamma-ray bursts \(629\)](#)

*Supporting material:* machine-readable tables

## 1. Introduction

Between 1994 November and 2021 August, the Konus-Wind (KW) gamma-ray spectrometer (Aptekar et al. 1995) on board the Global Geospace Science Wind spacecraft (s/c) detected 3394 gamma-ray bursts (GRBs) in the triggered mode, 495 of which were classified as short-duration gamma-ray bursts (sGRBs) or short bursts with extended emission (EE); see Svinkin et al. (2016, 2019) for the KW short/long GRB classification criteria.

Here we present the localization data obtained by arrival-time analysis, or “triangulation”, between the s/c in the 3rd InterPlanetary Network (IPN) for 199 sGRBs that occurred during the period from 2011 January 1 to 2021 August 31. The IPN localizations for 296 KW sGRBs detected in 1994–2010 have been presented earlier (Pal’shin et al. 2013, hereafter P13). Due to KW’s continuous coverage (duty cycle  $\gtrsim 95\%$ ) of the full sky by two omnidirectional detectors over a wide energy range ( $\sim 20$ – $15$  MeV), the KW sample is the most complete set of sGRBs with fluences above  $\sim 10^{-6}$  erg cm $^2$  s $^{-1}$  available to date.

The sGRB sample is not homogeneous: it includes both Type I (merger-origin) and Type II (collapsar-origin) GRBs; see Zhang et al. (2009) for more information on the Type I/II classification scheme. Taking into account the burst durations and hardness ratios (Svinkin et al. 2016, 2019), we estimate that about 20% of the bursts in our sample can be in fact Type II, or at least their classification as Type I is questionable. The sample also includes three possible sGRBs with EE.

Recently, rapid IPN localizations have facilitated significant discoveries in the GRB field, e.g., the localization of the short GRB 170817A, the counterpart of the gravitational-wave event GW170817 from a binary neutron star merger (Abbott et al. 2017), the detection of the extragalactic magnetar giant flare (MGF) in NGC 253 (Svinkin et al. 2021), and the discovery and confirmation of the shortest GRB from a collapsar (Ahumada et al. 2021). This catalog provides essential information for gravitational wave and neutrino searches from sGRBs, and for searches for extragalactic MGFs.

The novel feature of this catalog is the presentation of the final GRB localizations as probability sky maps using the Hierarchical Equal Area isoLatitude Pixelization (HEALPix<sup>41</sup>) discretization (Górski et al. 2005; Zonca et al. 2019). Since HEALPix has been recently accepted as a standard data format for multimessenger astronomy, such localizations will aid the joint analysis of localizations involving gravitational-wave observatories, as well as ground- and space-based facilities across the electromagnetic spectrum.

This catalog is organized as follows. In Section 2 we describe the composition of the IPN in 2011–2021 and briefly discuss the instrumentation and GRB observations. In Section 3 we provide triangulation annuli, other localization constraints used, and the methodology of deriving IPN error regions. Section 4 presents the final IPN error regions and discusses the statistics of the localizations; in Section 5 we give our conclusions. A

description of the data used and localization file format can be found in Appendices A and B, respectively. All coordinates are aberration-corrected equinox J2000.

## 2. Observations

The composition of the missions and experiments comprising the IPN changes as old missions are terminated and new missions are introduced. During the period covered in the present catalog (2011–2021), the IPN contained between seven and nine missions: KW, in orbit around the Lagrangian point  $L_1$ ; Mars Odyssey (a gamma-ray spectrometer, GRS, that includes the High-Energy Neutron Detector, HEND, with GRB detection capabilities; Hurley et al. 2006), in orbit around Mars; the Mercury Surface, Space Environment, Geochemistry, and Ranging mission (MESSENGER); the Gamma-Ray and Neutron Spectrometer (GRNS; Gold et al. 2001), in an eccentric orbit around Mercury; the International Gamma-Ray Laboratory (INTEGRAL; the anticoincidence shield of the spectrometer SPI (SPI-ACS), in an eccentric Earth orbit; Rau et al. 2005); RHESSI and the array of germanium detectors (GeD; Smith et al. 2002); the Neil Gehrels Swift Observatory (the Burst Alert Telescope, BAT; Gehrels et al. 2004); the Fermi Gamma-ray Space Telescope’s Gamma-Ray Burst Monitor (GBM; Meegan et al. 2009); the Suzaku mission (the Wide-band All-sky Monitor, WAM; Takahashi et al. 2007; Yamaoka et al. 2009); the Astro-rivelatore Gamma a Immagini LEggero mission (AGILE); the Mini-Calorimeter (MCAL; Tavani et al. 2009); the CALorimetric Electron Telescope on board the International Space Station (CALET); the Gamma-ray Burst Monitor (Yamaoka et al. 2013); the Hard X-ray Modulation Telescope (Insight-HXMT); the High-energy X-ray Telescope, HE; Zhang et al. 2020); and the Gravitational Wave High-energy Electromagnetic Counterpart All-sky Monitor (GECAM; gamma-ray detectors, GRDs; Chen et al. 2021; GECAM consists of two microsatellites, GECAM-A and GECAM-B, but currently only GECAM-B is in operation); all in low-Earth orbit. Table 1 lists the operation period, the distance from the Earth, the time resolution, the energy range of the detector used for triangulation, and the number of KW sGRBs observed by each mission/instrument.

For each KW sGRB we searched for detections in the data of the IPN s/c taking into account the possible range of propagation time delays. For each instrument we searched for a corresponding trigger or waiting-mode detection (if available from the instrument team). For CALET we used triggered events reported via the Gamma-ray Burst Coordinates Network<sup>42</sup> (GCN) only. Appendix A provides the instrument data sources and supplementary information.

Table 2 lists the 199 KW sGRBs observed by the IPN. The first column gives the burst designation, “GRBYYYYMMDD\_Tsssss”, where YYYYYMMDD is the burst date, and sssss is the KW trigger time (s, UT) truncated to integer seconds (note that, due to Wind’s large distance from Earth, this trigger time can differ by up to  $\sim 5.6$  s from the near-Earth s/c detection times). The second

<sup>41</sup> <https://healpix.sourceforge.io>

<sup>42</sup> <https://gcn.gsfc.nasa.gov/>

**Table 1**  
IPN Composition in 2011–2021

Mission (Instrument) <sup>a</sup>	Designation	Operation Period	Earth Distance <sup>b</sup> (lt-s)	Energy Band <sup>c</sup> (keV)	Time Resolution <sup>d</sup> (ms)	$N_{\text{GRBs}}$ <sup>e</sup>
Wind (Konus)	KW	Since 1994	Up to $\sim 6$	80–1500	2–256 (T)	199
INTEGRAL (SPI-ACS)	INT	Since 2002	Up to $\sim 0.5$	75–8000	50 (R)	164
Swift (BAT)	SWI	Since 2004	LEO	25–350	64 (R), TTE (T)	128
Fermi (GBM)	FER	Since 2008	LEO	80–1000	TTE (T)	113
AGILE (MCAL)	AGI	Since 2007	LEO	$\gtrsim 400$	TTE (T)	52
Suzaku (WAM)	SUZ	2005–2015	LEO	110–5000	1/64 s (T)	37
Insight-HXMT (HE)	INS	Since 2017	LEO	200–3000	TTE (T)	35
RHESSI (GeD)	RHE	2002–2018	LEO	$\gtrsim 100$	TTE	27
ISS (CALET-CGBM)	CAL	Since 2015	LEO	$\gtrsim 40$	TTE (T)	15
GECAM-B (GRD)	GEC	Since 2020	LEO	10–5000	TTE (T)	1
Mars Odyssey (HEND)	MO	Since 2001	Up to $\sim 1250$	50–3000	250 (R)	72
MESSENGER (GRNS)	MES	2004–2015	Up to $\sim 700$	40–200	1000 (T)	47

**Notes.**

<sup>a</sup> Instruments providing burst localizations, but not used for the triangulation: Fermi Large Area Telescope (LAT), Swift X-ray Telescope (XRT).

<sup>b</sup> Light travel time from the s/c to the Earth center; LEO: low-Earth orbit.

<sup>c</sup> Energy range used for triangulations.

<sup>d</sup> TTE stands for time-tagged event data. In parentheses the detection mode is given: T, trigger; R, waiting-mode rate increase.

<sup>e</sup> Number of Konus short bursts observed by each mission (for KW, the total number of bursts is given).

**Table 2**  
IPN/Konus Short Gamma-Ray Bursts

Designation	Konus-Wind Trigger Time (UT)	Name <sup>a</sup>	Type	Observed by <sup>b</sup>
GRB20110212_T47551	13:12:31.101	...	I	INT(R), SWI(R), SUZ(T), AGI(T), FER(T)
GRB20110221_T18490	05:08:10.017	...	I	MO(R), RHE(R), INT(R), SUZ(T), AGI(T)
GRB20110323_T57460	15:57:40.228	...	I	INT(R), SUZ(T)
GRB20110401_T79461	22:04:21.937	GRB 110401A	I/II	INT(R), SWI(R), AGI(T), FER(T)
GRB20110510_T80844	22:27:24.326	...	I/II	MES(T), MO(R), SWI(R)

**Notes.**

<sup>a</sup> As provided in the GCN circulars, if available.

<sup>b</sup> AGI: AGILE (MCAL); CAL: International Space Station CALET Gamma-ray Burst Monitor; GEC: GECAM-B (GRD); FER: Fermi (GBM); INS: Insight-HXMT (HE); INT: INTEGRAL (SPI-ACS); KON: Wind (Konus); LAT: Fermi (LAT); MES: MESSENGER (GRNS); MO: Mars Odyssey (HEND); RHE: RHESSI (GeD); SUZ: Suzaku (WAM); SWI: Swift (BAT). In parentheses the detection mode is given: T, trigger; R, rate increase.

(This table is available in its entirety in machine-readable form.)

column gives the KW trigger time in the standard time format. The “Name” column specifies the GRB name as provided in the GCN circulars, if available. The “Type” column specifies the burst type following the classification given in Svinkin et al. (2016, 2019). The types are as follows: I (merger origin), II (collapsar origin), I/II (the type is uncertain), Iee (type I with EE), and Iee/II (the type is uncertain: Iee or II). The “Observed by” column lists the missions/instruments which observed the burst.

We found that 198 of 199 KW sGRBs were observed by at least one other IPN s/c, enabling their localizations to be constrained by triangulation. The detections are given in Table 2 and are also available on the IPN website.<sup>43</sup> In total, 164 ( $\sim 82\%$ ) GRBs were observed by INTEGRAL, 185 ( $\sim 92\%$ ) by any near-Earth s/c, and 119 ( $\sim 60\%$ ) by distant s/c (Mars Odyssey and/or MESSENGER): 24 by two distant s/c and 95 by one distant s/c; 27 bursts were precisely localized by Swift-BAT or XRT (including GRB 150831A, which was also localized by INTEGRAL-IBIS/ISGRI). The

statistics of the events detected by each s/c are given in Table 1.

### 3. Localizations

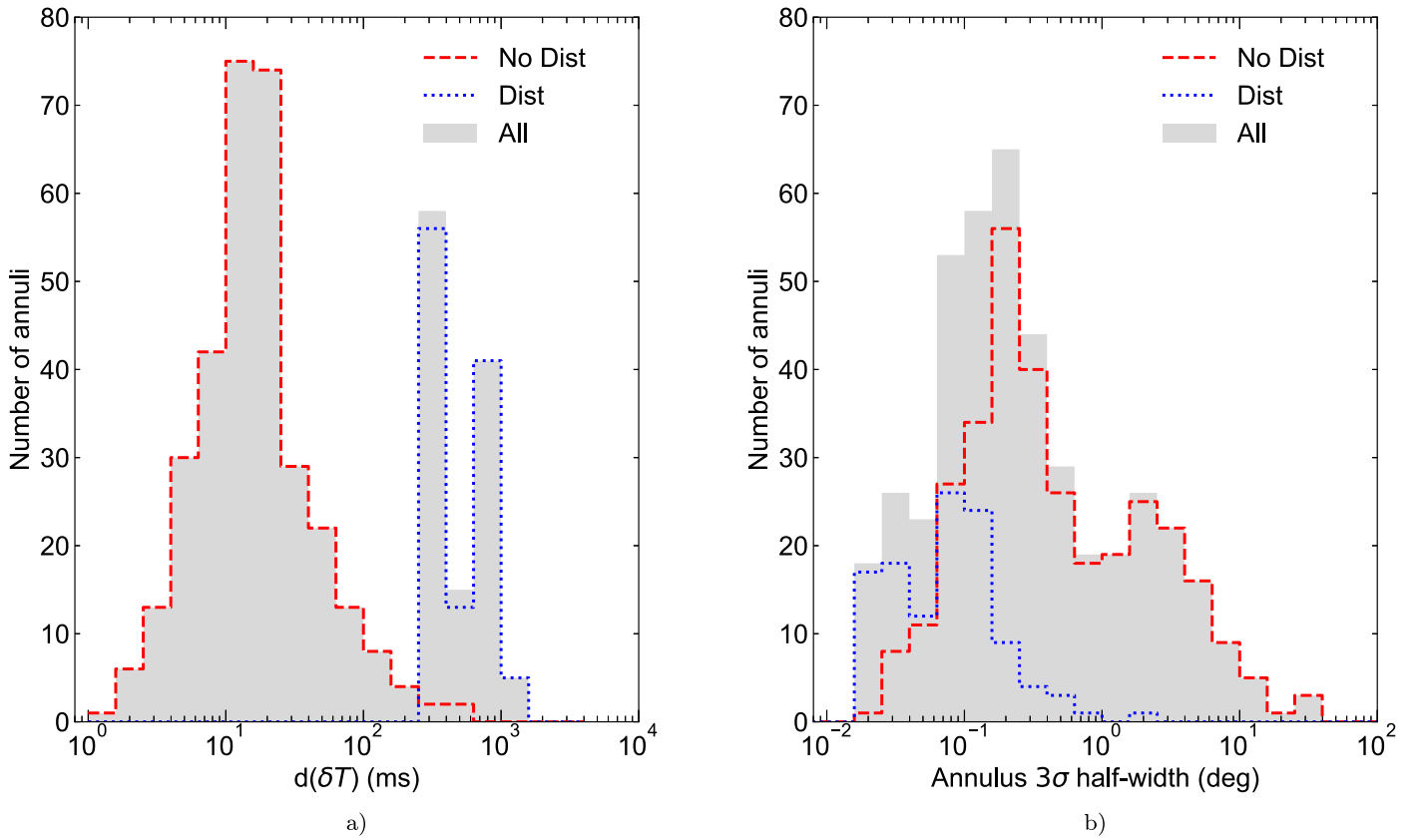
#### 3.1. Triangulation Annuli

Using a triangulation technique identical to that of P13 one or more triangulation annuli have been obtained for 198 KW short bursts.

From about 500 derived annuli, 435 were used in the catalog (including 115 annuli with distant s/c). For each burst we selected the annuli which form the smallest error region. Figure 1 shows the distributions of uncertainties in time delays and  $3\sigma$  half-widths of these annuli.

The detectors in the IPN vary widely in shape, composition, time resolution, and energy range. Also, onboard timekeeping techniques and accuracies differ from mission to mission, and s/c ephemeris data are given only as predictions for most missions. A detailed discussion of triangulation systematic effects is given in Hurley et al. (2017). Since the accuracy of the triangulation technique

<sup>43</sup> <http://ssl.berkeley.edu/ipn3/masterli.txt>



**Figure 1.** Distributions of uncertainties in time delay  $d(\delta T) = (d_+(\delta T) + |d_-(\delta T)|)/2$  (left) and  $3\sigma$  half widths (HWs, right) of the 438 triangulation annuli. Blue dotted lines: 115 annuli involving at least one distant s/c; red dashed lines: 323 annuli not involving any distant s/c. For annuli obtained using the KW and near-Earth (or INTEGRAL) s/c data, the smallest  $d(\delta T)$  is 1.2 ms, the largest is 600 ms, the mean is 29 ms, and the geometric mean is 16 ms; the smallest HW is  $0^{\circ}021$  ( $1/3$ ), the largest is  $36^{\circ}7$ , the mean is  $1^{\circ}6$ , and the geometric mean is  $0^{\circ}45$ . For annuli involving distant s/c, the smallest  $d(\delta T)$  is 361 ms, the largest is 1168 ms, the mean is 596 ms, and the geometric mean is 544 ms; the smallest HW is  $0^{\circ}016$  ( $0/9$ ), the largest is  $2^{\circ}1$ , the mean is  $1^{\circ}12$ , and the geometric mean is  $0^{\circ}72$ .

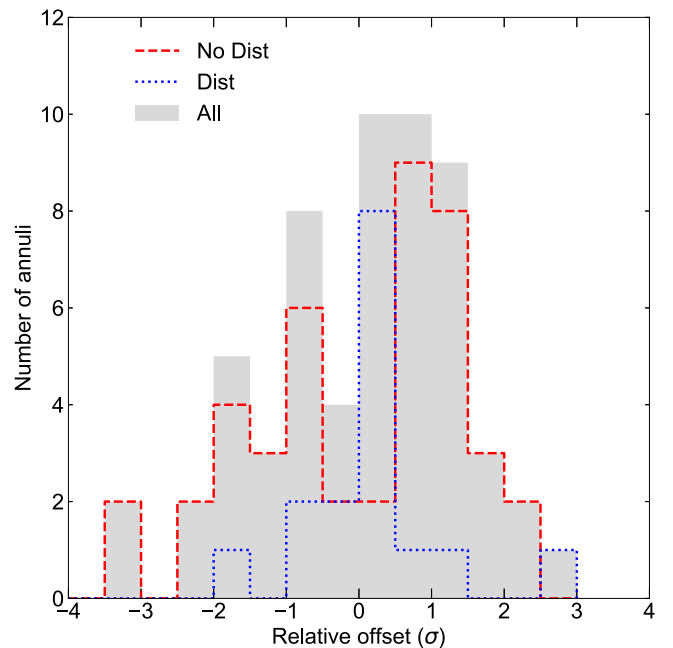
depends on all these parameters, end-to-end calibrations and sensitivity checks are a constant necessity.

### 3.2. Verifying Triangulation Annuli

Of the bursts localized by IPN, 27 were precisely localized by Swift-BAT or XRT (including GRB 150831A, which was also localized by INTEGRAL-IBIS/ISGRI). We utilized these bursts to verify our triangulations.

For these 27 bursts, 43 KW–near-Earth s/c (including 20 KW–INTEGRAL) and 16 KW (or Fermi)–distant s/c annuli were obtained. The Swift localizations were taken from either the Swift (XRT) catalog<sup>44</sup>, if an X-ray afterglow was found, or the third Swift (BAT) catalog (Lien et al. 2016). For recent GRBs, the BAT localizations were taken from GCN circulars with refined positions. In each case the triangulation annuli are in agreement with the precise Swift localization of the source, thereby confirming the reliability of our triangulations. A maximum offset of  $3.3\sigma$  was found for the bright GRB 130603B; for this burst, it corresponds to  $\sim 1$  ms systematic uncertainty in time delay.

Figure 2 shows the distributions of relative source offsets (in  $\sigma$ ) from the center lines of 43 KW–near-Earth s/c (including 20 KW–INTEGRAL) and 16 KW (or Fermi)–distant s/c annuli.



**Figure 2.** Distributions of relative offsets (in  $\sigma$ ) of the 27 precise GRB positions from the center lines of the IPN annuli. Red dashed line: 43 KW–near-Earth s/c (including 20 KW–INTEGRAL) annuli; blue dotted line: 16 KW (or Fermi)–distant s/c annuli.

<sup>44</sup> [https://www.swift.ac.uk/xrt\\_positions](https://www.swift.ac.uk/xrt_positions)

For these subsamples, the mean offsets are 0.0 and 0.2; the standard deviations are 1.4 and 0.9, respectively.

### 3.3. Additional Constraints

In addition to triangulation annuli, several other types of localization information are included in this catalog. They are ecliptic latitude range, autonomous burst localizations obtained by Fermi (GBM and LAT) or GECAM, and Earth or Mars blocking (MESSENGER was in an eccentric orbit around Mercury, so Mercury blocking was quite rare). This additional information helps to constrain the triangulation position, i.e., to choose one of two triangulation boxes, or to eliminate portions of a single annulus. In some cases the position of the BAT-coded field of view may constrain burst localization. In case a burst produced a significant ( $\gtrsim 5\sigma$ ) response in the BAT-summed array-rate light curve in the 15–350 keV energy band (see, e.g., Tohuvavohu et al. 2020 for the BAT data product description) and no BAT trigger was reported, the burst was most probably located outside the coded field of view of the BAT. Precise burst localizations by Swift-BAT or XRT are provided for verification of the IPN localizations.

#### 3.3.1. Ecliptic Latitudes

The ecliptic latitudes of the bursts are derived by comparing the count rates of the two KW detectors (S1 and S2) mounted on the opposite faces of the rotationally stabilized Wind s/c. The axis of S2 points toward the north ecliptic pole, and the axis of S1 points toward the south ecliptic pole.

The triggered mode data are available from a single KW detector, typically the one with a smaller GRB incidence angle ( $< 90^\circ$ ). Intense GRBs produce count-rate increases in the waiting-mode time history of both KW detectors measured with 2.944 s time resolution. The lack of a reliable Wind mass model and the s/c rotation do not allow us to directly derive the Wind incidence angle (the source ecliptic latitude) in a way similar to the Fermi (GBM) and GECAM burst-location techniques. Nevertheless, it is possible to estimate the source ecliptic latitude from the ratio of  $\sim 80$ –350 keV count rates in S1 and S2, calibrated using a sample of well-localized GRBs.

The ecliptic latitude range, namely the best estimate,  $\beta$ , and the lower and upper limits,  $\beta_{\min}$  and  $\beta_{\max}$ , can be considered to be an annulus centered at the north pole, with a half-angle  $\theta = 90^\circ - \beta$  and half-width  $d_-(\theta) = \beta - \beta_{\max}$ ,  $d_+(\theta) = \beta - \beta_{\min}$ . The ecliptic latitude uncertainty is estimated at the 99.73% ( $3\sigma$ ) confidence level.

#### 3.3.2. Planet Blocking

When a s/c in low-Earth or Martian orbit detects a burst, planet blocking may constrain burst localization, since the source position must be outside the occulted part of the sky. Since Fermi (GBM) has a higher sensitivity than KW across the unocculted sky it is possible to use GBM nondetections to constrain GRB positions. In this case the burst source is inside the Fermi Earth-occulted region. To check that the GBM is switched on and collecting data we use GBM POSHIST and CTIME data.

The allowed part of the sky is specified in the catalog as a degenerate annulus centered at the s/c's nadir vector, with a half-angle  $\theta = \arcsin(R_{\text{planet}}/R)$ , where  $R$  is the radius of the s/c orbit and  $R_{\text{planet}}$  is the solid planet radius assuming a spherical shape. The annulus half-widths are  $d_-(\theta) = -\theta$ ,

$d_+(\theta) = 0$ , in case the burst was occulted by the planet for the s/c, and  $d_-(\theta) = 0$ ,  $d_+(\theta) = 180^\circ - \theta$  in the opposite case.

#### 3.3.3. Autonomous Localizations

The autonomous localizations, derived by comparing the count rates of several detectors with a cosine-like angular response, are affected by Earth's albedo and absorption or scattering in the s/c structure, among other things; as a result, their shapes are rather complex. To produce the final IPN localization region we use GBM RoboBA localizations (Goldstein et al. 2020) in the HEALPix format publicly available for bursts since 2018; pre-2018 RoboBA localizations were provided for this work by the GBM team.

The error circles provided in GBM GRB catalogs (e.g., von Kienlin et al. 2020), are simple approximations to these shapes. They are centered at the most likely arrival direction for the burst, and their radii are defined as an average distance to the true 68% statistical-only error contour (Connaughton et al. 2015). In this catalog, in cases where GBM localizations constrain the burst location, we provide the GBM error circles for reference. For GRB20210307\_T21404 (the only burst in the catalog detected by GECAM) we provide the GECAM localization.

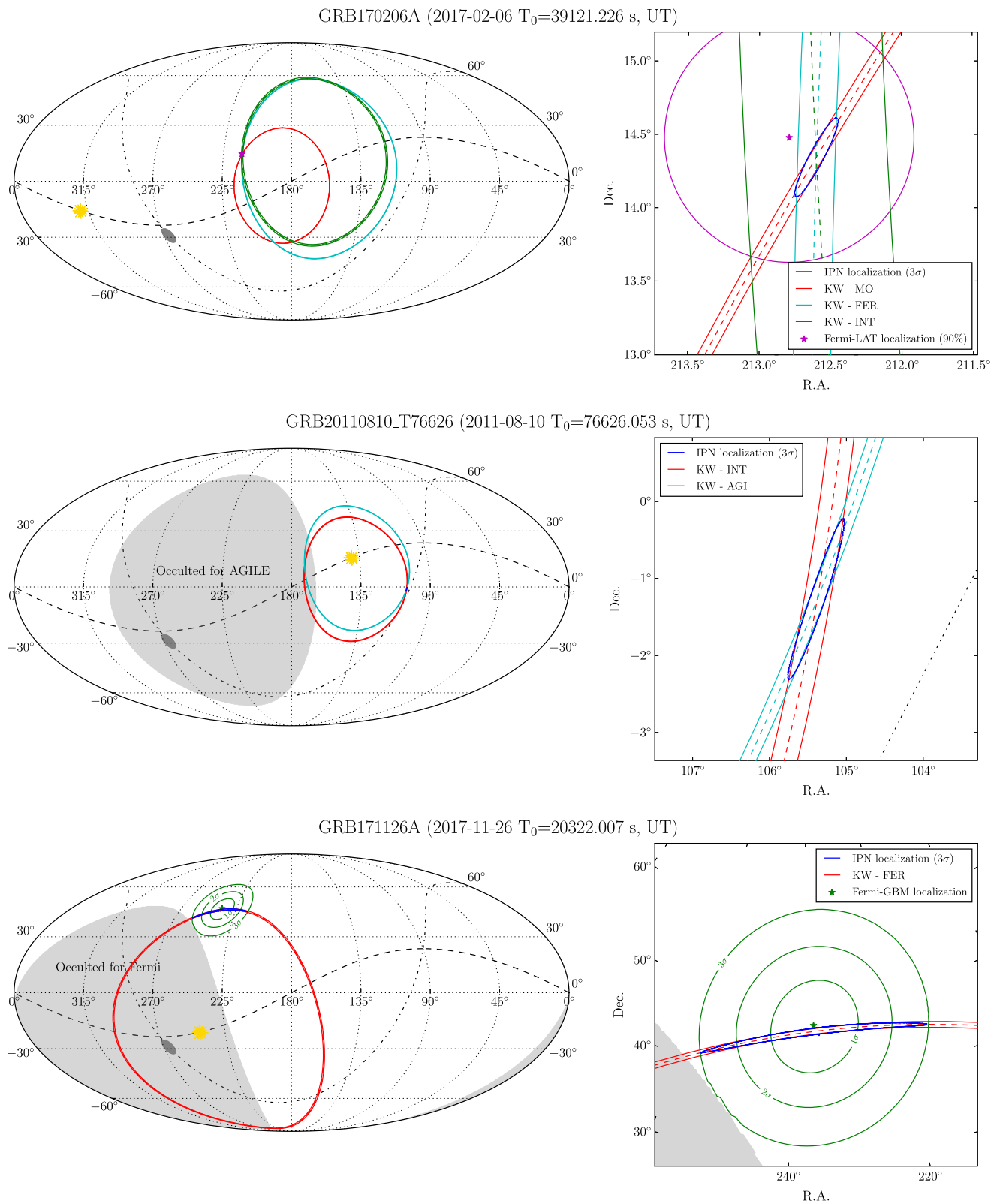
Fermi (LAT) localizations provided in the catalog are circles centered at the LAT best-reconstructed position with 90% containment radius (statistical only) and were taken from either the Fermi (LAT) catalog (Ajello et al. 2019) or, for recent GRBs, from GCN circulars.

### 3.4. Localization Regions

The final localizations were produced using the set of IPN annuli and additional constraints. For those bursts which were detected by three or more well-separated s/c, a small localization region (down to tens of arcmin<sup>2</sup>) can be derived (Figure 3, top panel). For such bursts, we have typically provided three annuli in the catalog. We used the two of them which provided the most compact localization region to construct the localization. As a typical result two regions are produced and, with the help of the third annulus, we selected the final region.

For bursts not observed by any distant s/c, but observed by KW, INTEGRAL (SPI-ACS), and one or more near-Earth s/c, the localization region is formed by the intersections of the KW–near-Earth s/c annulus and an INTEGRAL–near-Earth s/c annulus, or by a KW–near-Earth s/c annulus and a KW–INTEGRAL annulus intersecting at grazing incidence. In this case the final region was selected taking into account additional constraints (Figure 3, middle panel). Where a GBM localization is used we exclude a region if it lies outside the GBM  $3\sigma$  contour (calculated using the RoboBA localization). We also used Fermi (LAT) and precise Swift localizations (where available) for region selection.

For those bursts which were detected only by KW and one other s/c, or by KW and one or more near-Earth s/c, the resulting localization is formed by a triangulation annulus (the narrowest in the case of several KW–near-Earth s/c annuli) and additional constraints. These localizations consist of the entire annulus (in the case where it is entirely inside the allowed ecliptic latitude band and there are no other constraints) or one or two annulus segments, formed by the intersection of the annulus with the ecliptic latitude band, and/or by exclusion of



**Figure 3.** IPN localizations. The three panels present typical cases of IPN localization: GRB detected by four well-separated s/c (top panel); GRB detected by three s/c with an additional constraint used to select the final localization (middle panel); GRB detected by two s/c, the localization is formed by a single annulus and GBM localization (bottom panel). The left plot in each panel shows the whole sky with triangulation annuli and other constraints along with the ecliptic plane (dashed line) and Sun position at the GRB time; the Galactic plane (dashed–dotted line) and the Galactic center. The right plots are magnification insets showing the  $3\sigma$  localization confidence region (blue solid line). The GRB name and the KW trigger time are given in the figure title.

**Table 3**  
IPN Localization Data

Designation	$N$	Location Source	R.A. (deg)	Decl. (deg)	$\theta$ (deg)	$d_-(\theta)$ (deg)	$d_+(\theta)$ (deg)
GRB20110212_T47551	3	KW-FER	326.1161	-19.9156	54.4586	-0.0677	+0.0676
		KW-INT	324.7813	-25.3330	49.3296	-0.2804	+0.1747
		Pos.GBM	311.330	-74.500	4.33		
GRB20110221_T18490	3	KW-MO	330.8868	-13.0377	16.0404	-0.0657	+0.0692
		KW-SUZ	343.4756	-13.1519	27.6975	-0.2354	+0.4076
		KW-INT	342.3842	-20.1351	29.0384	-0.1671	+0.3316
GRB20110323_T57460	2	KW-SUZ	24.7970	9.8654	20.4803	-0.4630	+0.1954
		KW-INT	24.5553	5.7015	17.2516	-0.4805	+0.9990
GRB20110401_T79461	3	KW-INT	211.5140	-12.0493	63.8888	-0.2219	+0.1969
		FER-INT	91.5378	68.7932	85.6387	-2.1886	+3.1509
		Occ.SWI	115.940	20.532	66.440	-0.0	+113.560
GRB20110510_T80844	3	KW-SWI	228.2411	-23.4898	84.5588	-0.2262	+0.1233
		KW-MO	27.6375	10.6619	73.0224	-0.0246	+0.0246
		KW-MES	22.7559	6.0257	66.3059	-0.1203	+0.1179

(This table is available in machine-readable form.)

**Table 4**  
IPN Error Regions

Designation	$N_r$	R.A. (deg)	Decl. (deg)	Max. Dim. (deg)	Min. Dim. (deg)	Area (deg <sup>2</sup> )
GRB20110212_T47551	2	271.471	-57.147	12.745	0.135	1.534
		348.236	-72.931	12.745	0.135	1.534
GRB20110221_T18490	1	316.305	-5.895	3.406	0.135	0.413
GRB20110323_T57460	2	10.195	-4.350	12.197	0.658	6.496
		37.705	-5.885	12.197	0.658	6.494
GRB20110401_T79461	1	264.968	+24.902	6.948	0.419	2.955
GRB20110510_T80844	1	334.020	-43.873	3.216	0.050	0.131

(This table is available in machine-readable form.)

the occulted part of the annulus, or by combination with the GBM localization (Figure 3, bottom panel).

### 3.4.1. Probability Sky Maps

Localization maps were produced in the multiresolution map HEALPix format<sup>45</sup> using the `mhealpy` Python package<sup>46</sup> in the following way. The probability density for the annulus was specified by a Gaussian distribution centered at the symmetrized annulus center line and having  $3\sigma$  half-width equal to the annulus half-width. Localization annuli are typically asymmetrical with respect to the annulus center line; they are symmetrized by defining an average annulus half-width about a displaced center line. The planet-blocking regions were specified by a degenerate annulus on the sky with a uniform probability inside it and zero probability outside; see Section 3.3.2.

In case a burst was detected by BAT outside the coded field of view, the BAT-coded field of view was represented as a region with partial coding fraction  $>10\%$  with zero probability inside it. The KW ecliptic latitude band was represented as an annulus with a uniform probability inside it and zero probability outside, centered at the north ecliptic pole with

radius and half-width corresponding to the incident angle constraint. The final probability density was calculated as a product of the selected annuli and constraints.

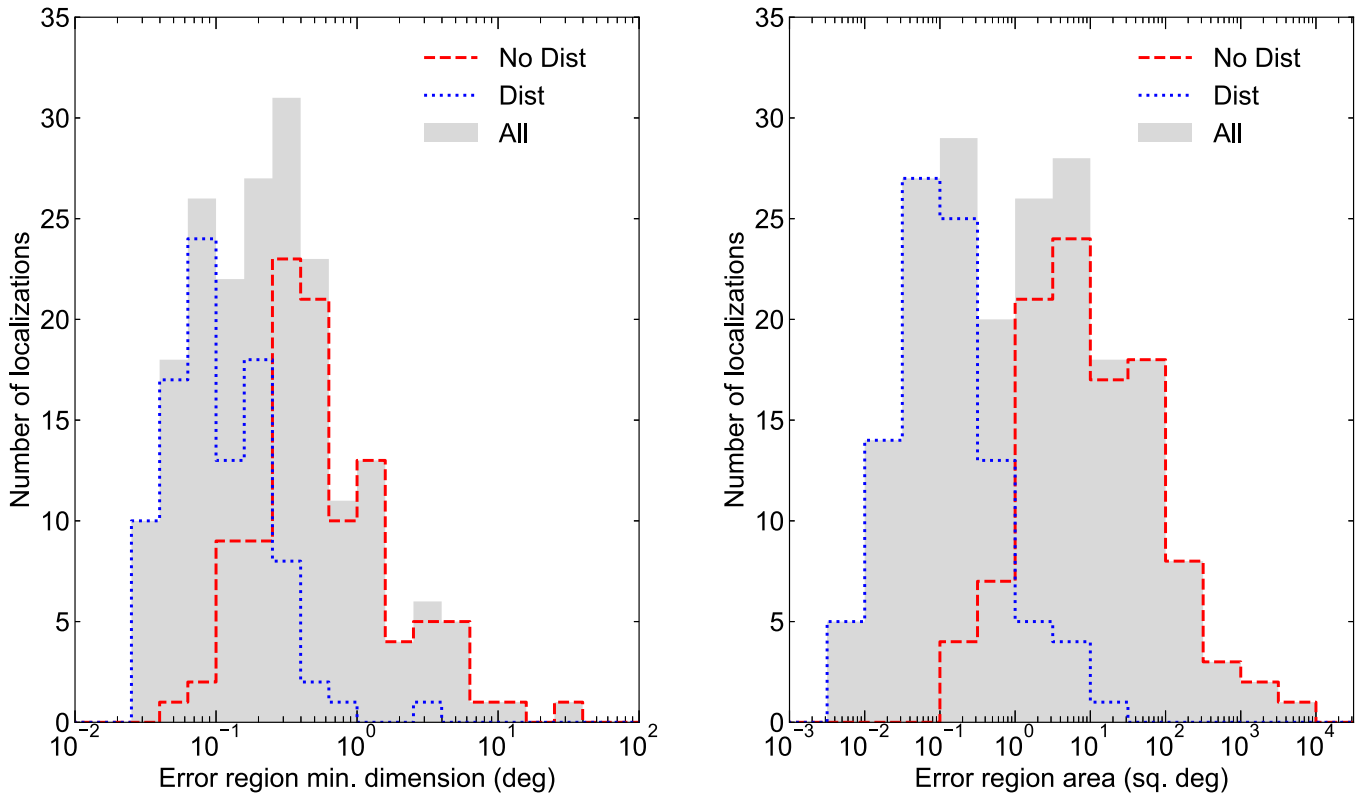
We note that, in this work, the probability densities for each annuli are assumed to be independent, despite that they may involve overlapping data (e.g., in case of intersection of KW-FER and FER-INT annuli). Such simplification can be avoided in future with more sophisticated methods (e.g., Burgess et al. 2021).

The localization contours were calculated using the `ligo.skymap` package<sup>47</sup>, modified for the multiresolution map case. Examples of the localization maps are given in Figure 3. The probability sky maps are stored in files following the Flexible Image Transport System (FITS) standard (see Appendix B for file description).

## 4. Localizations: Results

Table 3 summarizes localization information for 199 Konus short bursts. The first column gives the burst designation (see Table 2). The second column gives the number of localization constraints (the number of rows with localization information for the burst). The six subsequent columns give localizations

<sup>45</sup> <https://www.ivoa.net/documents/MOC><sup>46</sup> <https://mhealpy.readthedocs.io><sup>47</sup> <https://lscsoft.docs.ligo.org/ligo.skymap>



**Figure 4.** Distributions of minimum sizes (left) and areas (right) of the IPN localizations. Blue dotted lines: 94 Konus short bursts observed by at least one distant s/c; red dashed lines: 105 bursts not observed by any distant s/c. The minimum region dimensions range from  $0^{\circ}033$  ( $2'0$ ) to  $3^{\circ}32$  with a mean of  $0^{\circ}17$ , and a geometric mean of  $0^{\circ}11$  (for bursts observed by distant s/c) and from  $0^{\circ}043$  ( $2'6$ ) to  $36^{\circ}5$  with a mean of  $1^{\circ}5$ , and a geometric mean of  $0^{\circ}6$  (for bursts without distant s/c detections). The areas range from  $0.005 \text{ deg}^2$  ( $18 \text{ arcmin}^2$ ) to  $14.4 \text{ deg}^2$  with a mean of  $0.70 \text{ deg}^2$ , and a geometric mean of  $0.12 \text{ deg}^2$  (for bursts observed by distant s/c) and from  $0.156 \text{ deg}^2$  to  $3163 \text{ deg}^2$  with a mean of  $103 \text{ deg}^2$ , and a geometric mean of  $11.0 \text{ deg}^2$  (for bursts without distant s/c detections).

expressed as a set of annuli: the third column gives the source of the location: either sc1–sc2 (triangulation annulus derived using sc1 and sc2), or “Ecl.Lat” (range of ecliptic latitudes), or “Pos.Instr” (“Instr” is one of the following: “SWI” for Swift-BAT or XRT, “GBM” or “LAT” for Fermi, and “GEC” for GECAM localizations), or “Occ.sc” (planet blocking for s/c); Columns 4–8 list the R.A. and decl. of the annulus center, the annulus radius  $\theta$ , and the  $3\sigma$  uncertainties in the radius  $d_-(\theta)$ ,  $d_+(\theta)$ . Planet blocking, ecliptic latitude range, and autonomous localizations are given only if they constrain the location.

Table 4 gives the description of the final IPN error regions (including the 27 imaged bursts). The nine columns contain the following information: (1) the burst designation (see Table 2); (2) the number of error regions for the burst,  $N_r$ : 1 or 2; (3) and (4) the R.A. and decl. of the most probable burst location for each region; (5) the maximum dimension of the region (that is, the maximum angular distance between two points at the 99.73% probability region boundary); (6) the minimum dimension of the region (that is, the full-width of the narrowest annulus forming the region); (7) the area (for two regions the area of each region) enclosing 99.73% probability. Distributions of the region dimensions and areas are shown in Figure 4.

## 5. Conclusions

This paper continues a series of catalogs of GRB localizations obtained by arrival-time analysis, or “triangulation”, between the s/c in the 3rd IPN, as summarized in Table 5. We have presented the most comprehensive IPN localization data on 199 KW short bursts detected between 2011 January 1 and 2021 August 31.

**Table 5**  
IPN Catalogs of Gamma-Ray Bursts to Date

Years Covered	Number of GRBs	Description
1990–1992	16	Ulysses, Pioneer Venus Orbiter, WATCH, SIGMA, PHEBUS GRBs <sup>a</sup>
1990–1994	56	Granat-WATCH supplement <sup>b</sup>
1991–1992	37	Pioneer Venus Orbiter, Compton Gamma-Ray Observatory, Ulysses GRBs <sup>c</sup>
1991–1994	218	BATSE 3B supplement <sup>d</sup>
1991–2000	211	BATSE untriggered burst supplement <sup>e</sup>
1992–1993	9	Mars Observer GRBs <sup>f</sup>
1994–1996	147	BATSE 4Br supplement <sup>g</sup>
1994–2010	279	First Konus short bursts <sup>h</sup>
1996–2000	343	BATSE 5B supplement <sup>i</sup>
1996–2002	475	BeppoSAX supplement <sup>j</sup>
2000–2006	226	HETE-2 supplement <sup>k</sup>
2008–2010	146	First GBM supplement <sup>l</sup>
2010–2012	165	Second GBM supplement <sup>m</sup>
2011–2021	199	Second Konus short bursts <sup>n</sup>

**Notes.** <sup>a</sup> Hurley et al. (2000a); <sup>b</sup> Hurley et al. (2000b); <sup>c</sup> Laros et al. (1998); <sup>d</sup> Hurley et al. (1999a); <sup>e</sup> Hurley et al. (2005); <sup>f</sup> Laros et al. (1997); <sup>g</sup> Hurley et al. (1999b); <sup>h</sup> Pal’shin et al. (2013); <sup>i</sup> Hurley et al. (2011a); <sup>j</sup> Hurley et al. (2010); <sup>k</sup> Hurley et al. (2011b); <sup>l</sup> Hurley et al. (2013); <sup>m</sup> Hurley et al. (2017); <sup>n</sup> Present catalog.

With one exception, IPN localizations were obtained for these events (for GRB20171108\_T51656 observed by KW only, the source position is constrained to the Fermi Earth-occulted region



combined with the KW ecliptic latitude range). We verified the triangulations using 27 bursts localized by instruments with imaging capability. In each case the derived IPN annuli are in agreement with the precise GRB position, thereby confirming the reliability of our results.

Currently the nine-s/c IPN detects about 325 bursts per year (Hurley et al. 2017), about 18 of which are rather bright, short-duration, hard spectrum GRBs (see P13 and this work). The IPN localizations can be used for a wide variety of purposes, including, but not limited to, searches for gravitational waves, kilonovae, and neutrino signals from merging compact objects, very-high-energy photons from the burst sources, and giant magnetar flares in nearby galaxies. As KW continues to operate, we anticipate more localizations, in particular in conjunction with upcoming LIGO/Virgo operations.

D.S.S., A.V.R., A.L.L., D.D.F., and M.V.U. acknowledge support from RSF grant No. 21-12-00250. The HEND experiment was supported by the Russian State Corporation Roscosmos and implemented as part of the Gamma-Ray Spectrometer suite on NASA Mars Odyssey. HEND data processing was funded by the Ministry of Science and Higher Education of the Russian Federation, grant No. AAAA-A18-118012290370-6. KH is grateful for support under the Fermi Guest Investigator program, grant No. 80NSSC20K0585. We thank Valentin Pal'shin for his considerable contribution to the Konus-Wind and IPN data analysis tools. Some of the results in this paper have been derived using the healpy and HEALPix packages.

*Facilities:* Wind (Konus), Fermi (GBM and LAT), Swift (BAT and XRT), Suzaku (WAM), AGILE (MCAL), ISS (CALET-CGBM), Insight-HXMT (HE), GECAM-B, INTEGRAL (SPI-ACS), MESSENGER (GRNS), Mars Odyssey (HEND).

*Software:* Astropy (Astropy Collaboration et al. 2013, 2018); Fermi GBM Data Tools (Goldstein 2021); Utilities for Swift (BAT) instrument ([https://github.com/lanl/swiftbat\\_python](https://github.com/lanl/swiftbat_python)); Astroquery (Ginsburg et al. 2019); healpy (Górski et al. (2005); Zonca et al. (2019), <https://healpix.sourceforge.io>); mhealpy (<https://mhealpy.readthedocs.io>); ligo.skymap (<https://lscsoft.docs.ligo.org/ligo.skymap>).

## Appendix A Data Sources

### A.1. IPN Instrument Data

We use the following sources for the instrument data: Swift-BAT,<sup>48</sup> for recent GRBs we used BAT time-tagged event data that exist due to the Gamma-ray Urgent Archiver for Novel Opportunities (GUANO; Tohuvavohu et al. 2020); Fermi-GBM<sup>49</sup>; Suzaku-WAM<sup>50</sup>; INTEGRAL-SPI-ACS<sup>51</sup>; MESSENGER-GRNS<sup>52</sup>; AGILE-MCAL, Insight-HXMT, and Mars Odyssey HEND data are available on request from the instrument teams. The AGILE-MCAL sGRB data are part of the the Second AGILE-MCAL GRB Catalog (Ursi et al. 2022).

<sup>48</sup> <https://heasarc.gsfc.nasa.gov/FTP/swift/data/obs/>

<sup>49</sup> <https://heasarc.gsfc.nasa.gov/FTP/fermi/data/gbm/triggers/>

<sup>50</sup> [http://www.astro.isas.jaxa.jp/suzaku/HXD-WAM/WAM-GRB/grb/trig/grb\\_table.html](http://www.astro.isas.jaxa.jp/suzaku/HXD-WAM/WAM-GRB/grb/trig/grb_table.html)

<sup>51</sup> <http://isdc.unige.ch/~savchenk/spiacs-online/>

<sup>52</sup> <https://pds-geosciences.wustl.edu/missions/messenger/gms.htm>

### A.2. Ephemeris and Clock Accuracy Data

Near-Earth s/c ephemerides were derived from two-line elements (TLE) available at <https://www.space-track.org> using the SGP8 model. For Wind we use the predicted ephemeris; for the Mars Odyssey and MESSENGER ephemerides, and the Mars Odyssey nadir vectors, we used the JPL Horizons online ephemeris system<sup>53</sup> using the astroquery Python package (Ginsburg et al. 2019). INTEGRAL ephemeris data are available via the SPI-ACS data web interface. The Wind-predicted ephemeris data and their description are available at [https://spdf.gsfc.nasa.gov/pub/data/wind/orbit/pre\\_or/](https://spdf.gsfc.nasa.gov/pub/data/wind/orbit/pre_or/) and [https://cdaweb.gsfc.nasa.gov/misc/Notes/W.html#WI\\_OR\\_PRE](https://cdaweb.gsfc.nasa.gov/misc/Notes/W.html#WI_OR_PRE).

The declared onboard clock accuracy of the s/c are as follows: down to 1  $\mu$ s for Fermi;  $\sim$ 200  $\mu$ s for Swift;  $\sim$ 1 ms for Wind; and  $\sim$ 100  $\mu$ s for INTEGRAL; for Mars Odyssey an overall  $3\sigma$  systematic uncertainty, which includes timing and other effects derived from IPN observations of precisely localized GRBs, is better than 360 ms; the corresponding MESSENGER uncertainty is 800 ms. The Swift timing corrections were calculated using Swift-BAT utilities. The Wind clock drift information is provided at [https://pwgdata.sci.gsfc.nasa.gov/pub/wind\\_clock/](https://pwgdata.sci.gsfc.nasa.gov/pub/wind_clock/).

## Appendix B Localization Files

The localizations are stored in a series of FITS data files available online from the Ioffe website<sup>54</sup> in the following formats: multiresolution HEALPix maps (\*\_IPN\_map\_hpx\_moc.fits.gz) and regular resolution HEALPix maps (\*\_IPN\_map\_hpx.fits.gz). In addition to HEALPix maps the website stores the localization 0.9973 integrated probability contours in ASCII format, which contain the coordinates of the center of the pixel with the maximum probability (two pixels are given in the case of two localization regions), followed by the region contour coordinates; and plots produced using the ligo.skymap package.

The regular resolution maps are standard HEALPix FITS files with RING numeration, and celestial coordinate system. The single extension table of the file contains the pixel probability. The comment field contains information about the instruments involved in localization, a list of additional constraints, and the parameters of the IPN annuli used. The extension table of the multiresolution map file contains the pixel probability and the pixel index in the UNIQ indexing scheme<sup>55</sup> (Singer & Price 2016).




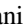

## ORCID iDs

- D. S. Svinkin  <https://orcid.org/0000-0002-2208-2196>  
 K. Hurley  <https://orcid.org/0000-0003-3315-1975>  
 A. V. Ridnaia  <https://orcid.org/0000-0001-9477-5437>  
 A. L. Lysenko  <https://orcid.org/0000-0002-3942-8341>  
 D. D. Frederiks  <https://orcid.org/0000-0002-1153-6340>  
 A. E. Tsvetkova  <https://orcid.org/0000-0003-0292-6221>  
 A. Goldstein  <https://orcid.org/0000-0002-0587-7042>  
 C. Wilson-Hodge  <https://orcid.org/0000-0002-8585-0084>

<sup>53</sup> <https://ssd.jpl.nasa.gov/horizons.cgi>

<sup>54</sup> [http://www.ioffe.ru/LEA/ShortGRBs\\_IPN/](http://www.ioffe.ru/LEA/ShortGRBs_IPN/)

<sup>55</sup> [https://emfollow.docs.ligo.org/userguide/tutorial/multiorder\\_skymaps.html](https://emfollow.docs.ligo.org/userguide/tutorial/multiorder_skymaps.html)

E. Burns  <https://orcid.org/0000-0002-2942-3379>  
 A. von Kienlin  <https://orcid.org/0000-0002-0221-5916>  
 A. Rau  <https://orcid.org/0000-0001-5990-6243>  
 V. Savchenko  <https://orcid.org/0000-0001-6353-0808>  
 E. Bozzo  <https://orcid.org/0000-0002-7504-7423>  
 C. Ferrigno  <https://orcid.org/0000-0003-1429-1059>  
 D. M. Palmer  <https://orcid.org/0000-0001-7128-0802>  
 A. Tohuvavohu  <https://orcid.org/0000-0002-2810-8764>  
 Y. Fukazawa  <https://orcid.org/0000-0002-0921-8837>  
 Y. Terada  <https://orcid.org/0000-0002-2359-1857>  
 K. Makishima  <https://orcid.org/0000-0002-1040-8769>  
 A. Ursi  <https://orcid.org/0000-0002-7253-9721>  
 M. Tavani  <https://orcid.org/0000-0003-2893-1459>  
 A. Bulgarelli  <https://orcid.org/0000-0001-6347-0649>  
 C. Casentini  <https://orcid.org/0000-0001-8100-0579>  
 E. Del Monte  <https://orcid.org/0000-0002-3013-6334>  
 F. Longo  <https://orcid.org/0000-0003-2501-2270>  
 N. Parmiggiani  <https://orcid.org/0000-0002-4535-5329>  
 C. Pittori  <https://orcid.org/0000-0001-6661-9779>  
 F. Verrecchia  <https://orcid.org/0000-0003-3455-5082>  
 S. Xiao  <https://orcid.org/0000-0003-2957-2806>  
 S. L. Xiong  <https://orcid.org/0000-0002-4771-7653>  
 I. Martinez-Castellanos  <https://orcid.org/0000-0002-2471-8696>

## References

- Abbott, B. P., Abbott, R., Abbott, T. D., et al. 2017, *ApJL*, **848**, L12  
 Ahumada, T., Singer, L. P., Anand, S., et al. 2021, *NatAs*, **5**, 917  
 Ajello, M., Arimoto, M., Axelsson, M., et al. 2019, *ApJ*, **878**, 52  
 Aptekar, R. L., Frederiks, D. D., Golenetskii, S. V., et al. 1995, *SSRv*, **71**, 265  
 Astropy Collaboration, Price-Whelan, A. M., Sipőcz, B. M., et al. 2018, *AJ*, **156**, 123  
 Astropy Collaboration, Robitaille, T. P., Tollerud, E. J., et al. 2013, *A&A*, **558**, A33  
 Burgess, J. M., Cameron, E., Svinkin, D., & Greiner, J. 2021, *A&A*, **654**, A26  
 Chen, C., Xiao, S., Xiong, S., et al. 2021, *ExA*, **52**, 45  
 Connaughton, V., Briggs, M. S., Goldstein, A., et al. 2015, *ApJS*, **216**, 32  
 Gehrels, N., Chincarini, G., Giommi, P., et al. 2004, *ApJ*, **611**, 1005  
 Ginsburg, A., Sipőcz, B. M., Brasseur, C. E., et al. 2019, *AJ*, **157**, 98  
 Gold, R. E., Solomon, S. C., McNutt, R. L., et al. 2001, *P&SS*, **49**, 1467  
 Goldstein, A., Cleveland, W. H., & Kocevski, D. 2021, Fermi GBM Data Tools: v1.1.0, <https://fermi.gsfc.nasa.gov/ssc/data/analysis/gbm>  
 Goldstein, A., Fletcher, C., Veres, P., et al. 2020, *ApJ*, **895**, 40  
 Górski, K. M., Hivon, E., Banday, A. J., et al. 2005, *ApJ*, **622**, 759  
 Hurley, K., Aptekar, R. L., Golenetskii, S. V., et al. 2017, *ApJS*, **229**, 31  
 Hurley, K., Atteia, J. L., Barraud, C., et al. 2011b, *ApJS*, **197**, 34  
 Hurley, K., Briggs, M. S., Kippen, R. M., et al. 1999a, *ApJS*, **120**, 399  
 Hurley, K., Briggs, M. S., Kippen, R. M., et al. 1999b, *ApJS*, **122**, 497  
 Hurley, K., Briggs, M. S., Kippen, R. M., et al. 2011a, *ApJS*, **196**, 1  
 Hurley, K., Guidorzi, C., Frontera, F., et al. 2010, *ApJS*, **191**, 179  
 Hurley, K., Laros, J., Brandt, S., et al. 2000a, *ApJ*, **533**, 884  
 Hurley, K., Lund, N., Brandt, S., et al. 2000b, *ApJS*, **128**, 549  
 Laros, J. G., Mitrofanov, I., Kozyrev, A., et al. 2006, *ApJS*, **164**, 124  
 Hurley, K., Pal'shin, V. D., Aptekar, R. L., et al. 2013, *ApJS*, **207**, 39  
 Hurley, K., Stern, B., Kommers, J., et al. 2005, *ApJS*, **156**, 217  
 Laros, J. G., Boynton, W. V., Hurley, K. C., et al. 1997, *ApJS*, **110**, 157  
 Laros, J. G., Hurley, K. C., Fenimore, E. E., et al. 1998, *ApJS*, **118**, 391  
 Lien, A., Sakamoto, T., Barthelmy, S. D., et al. 2016, *ApJ*, **829**, 7  
 Meegan, C., Lichti, G., Bhat, P. N., et al. 2009, *ApJ*, **702**, 791  
 Pal'shin, V. D., Hurley, K., Svinkin, D. S., et al. 2013, *ApJS*, **207**, 38  
 Rau, A., Kienlin, A. V., Hurley, K., & Lichti, G. G. 2005, *A&A*, **438**, 1175  
 Singer, L. P., & Price, L. R. 2016, *PhRvD*, **93**, 024013  
 Smith, D. M., Lin, R. P., Turin, P., et al. 2002, *SoPh*, **210**, 33  
 Svinkin, D., Frederiks, D., Hurley, K., et al. 2021, *Natur*, **589**, 211  
 Svinkin, D. S., Aptekar, R. L., Golenetskii, S. V., et al. 2019, *JPhCS*, **1400**, 022010  
 Svinkin, D. S., Frederiks, D. D., Aptekar, R. L., et al. 2016, *ApJS*, **224**, 10  
 Takahashi, T., Abe, K., Endo, M., et al. 2007, *PASJ*, **59**, 35  
 Tavani, M., Barbiellini, G., Argan, A., et al. 2009, *A&A*, **502**, 995  
 Tohuvavohu, A., Kennea, J. A., DeLaunay, J., et al. 2020, *ApJ*, **900**, 35  
 Ursi, A., Romani, M., Verrecchia, F., et al. 2022, *ApJ*, **925**, 152  
 von Kienlin, A., Meegan, C. A., Paciesas, W. S., et al. 2020, *ApJ*, **893**, 46  
 Yamaoka, K., Endo, A., Enoto, T., et al. 2009, *PASJ*, **61**, S35  
 Yamaoka, K., Yoshida, A., Sakamoto, T., et al. 2013, ICRC (Rio de Janeiro), **33**, 2948  
 Zhang, B., Zhang, B.-B., Virgili, F. J., et al. 2009, *ApJ*, **703**, 1696  
 Zhang, S.-N., Li, T., Lu, F., et al. 2020, *SCPMA*, **63**, 249502  
 Zonca, A., Singer, L., Lenz, D., et al. 2019, *JOSS*, **4**, 1298